Monthly Notices
of the
ROYAL ASTRONOMICAL SOCIETY

MNRAS **494,** 4090–4097 (2020)
Advance Access publication 2020 March 30

doi:10.1093/mnras/staa820

The [C II]/[N II] ratio in $3 < z < 6$ sub-millimetre galaxies from the South Pole Telescope survey

D. J. M. Cunningham [1,2★] S. C. Chapman,[2,3,4★] M. Aravena,[5] C. De Breuck,[6] M. Béthermin,[7] Chian-Chou Chen [6], Chenxing Dong,[8] A. H. Gonzalez [8], T. R. Greve,[9,10] K. C. Litke,[11] J. Ma,[8] M. Malkan,[12] D. P. Marrone,[11] T. Miller,[2,13] K. A. Phadke,[14] C. Reuter,[14] K. Rotermund,[2] J. S. Spilker,[15] A. A. Stark,[16] M. Strandet,[17,18] J. D. Vieira[14] and A. Weiß[17]

[1]*Department of Astronomy and Physics, Saint Mary's University, 923 Robie Street, Halifax, NS B3H 3C3, Canada*
[2]*Department of Physics and Atmospheric Science, Dalhousie University, 6310 Coburg Road, Halifax, NS B3H 4R2, Canada*
[3]*Herzberg Astronomy and Astrophysics Research Centre, National Research Council, 5071 West Saanich Road, Victoria, BC V9E 2E7, Canada*
[4]*Department of Physics and Astronomy, University of British Columbia, 6225 Agricultural Road, Vancouver, BC V6T 1Z1, Canada*
[5]*Núcleo de Astronomía, Facultad de Ingeniería, Universidad Diego Portales, Av. Ejército 441, Santiago, Chile*
[6]*European Southern Observatory, Karl Schwarzschild Straße 2, D-85748 Garching, Germany*
[7]*Laboratoire d'Astrophysique de Marseille (LAM), Aix Marseille University, CNRS, Marseille, France*
[8]*Bryant Space Science Center, Department of Astronomy, University of Florida, Gainesville, FL 32611, USA*
[9]*Department of Physics and Astronomy, University College London, Gower Street, London WC1E 6BT, UK*
[10]*Cosmic Dawn Center (DAWN), National Space Institute, Technical University of Denmark, DK-2800 Kgs. Lyngby, Denmark*
[11]*Steward Observatory, University of Arizona, 933 North Cherry Avenue, Tucson, AZ 85721, USA*
[12]*Department of Physics and Astronomy, University of California, Los Angeles, CA 90095-1547, USA*
[13]*Department of Astronomy, Yale University, 52 Hillhouse Avenue, New Haven, CT 06511, USA*
[14]*Department of Astronomy, University of Illinois, 1002 West Green St, Urbana, IL 61801, USA*
[15]*Department of Astronomy, University of Texas at Austin, 2515 Speedway, Stop C1400, Austin, TX 78712, USA*
[16]*Harvard–Smithsonian Center for Astrophysics, 60 Garden Street, Cambridge, MA 02138, USA*
[17]*Max-Planck-Institut für Radioastronomie, Auf dem Hügel 69, D-53121 Bonn, Germany*
[18]*International Max Planck Research School (IMPRS) for Astronomy and Astrophysics, Universities of Bonn and Cologne, Bonn, Germany*

Accepted 2020 March 19. Received 2020 March 15; in original form 2019 April 9

ABSTRACT

We present Atacama Compact Array and Atacama Pathfinder Experiment observations of the [N II] 205 μm fine-structure line in 40 sub-millimetre galaxies lying at redshifts $z = 3$–6, drawn from the 2500 deg^2 South Pole Telescope survey. This represents the largest uniformly selected sample of high-redshift [N II] 205 μm measurements to date. 29 sources also have [C II] 158 μm line observations allowing a characterization of the distribution of the [C II] to [N II] luminosity ratio for the first time at high redshift. The sample exhibits a median $L_{[\mathrm{C\,II}]}/L_{[\mathrm{N\,II}]} \approx 11.0$ and interquartile range of 5.0–24.7. These ratios are similar to those observed in local (Ultra)luminous infrared galaxies (LIRGs), possibly indicating similarities in their interstellar medium. At the extremes, we find individual sub-millimetre galaxies with $L_{[\mathrm{C\,II}]}/L_{[\mathrm{N\,II}]}$ low enough to suggest a smaller contribution from neutral gas than ionized gas to the [C II] flux and high enough to suggest strongly photon or X-ray region dominated flux. These results highlight a large range in this line luminosity ratio for sub-millimetre galaxies, which may be caused by variations in gas density, the relative abundances of carbon and nitrogen, ionization parameter, metallicity, and a variation in the fractional abundance of ionized and neutral interstellar medium.

Key words: galaxies: evolution – galaxies: high-redshift – galaxies: statistics – submillimetre: galaxies – submillimetre: ISM.

* E-mail: dcunningham@dal.ca (DJMC); scott.chapman@dal.ca (SCC)

1 INTRODUCTION

Observing far-infrared (FIR) luminous galaxies at high redshift is a crucial step in understanding the evolution of galaxies as they highlight periods of intense star formation that may represent pivotal growth periods in a galaxy's evolution (e.g. Casey, Narayanan & Cooray 2014). At $z \sim 2$, sub-millimetre galaxies (SMGs) may have accounted for 50 per cent of star formation in the Universe (Wardlow et al. 2011). At high redshift, the FIR emission from these galaxies peaks at sub-millimetre wavelengths in the observer's frame, allowing effective selection at sub-mm or longer wavelengths. The peak redshift at which they are predominantly found depends on the wavelength of the survey: at ∼850 μm, the peak is close to $z \sim 2.5$ (Chapman et al. 2003, 2005), while at the 1–2 mm regime of the South Pole Telescope (SPT) survey, the median redshift increases to $\langle z \rangle \sim 4$ (Weiß et al. 2013; Strandet et al. 2016). Regardless of wavelength of selection, they display rapid star formation sometimes exceeding $10^3\,M_\odot yr^{-1}$ (Swinbank et al. 2014), and have stellar masses of the order of $10^{11}\,M_\odot$ (Hainline et al. 2011; Michalowski, et al. 2012; Ma et al. 2015). Their rapid evolution early in cosmic time continues to push current simulations to match their detailed properties (e.g. Shimizu, Yoshida & Okamoto 2012; Hayward et al. 2013; Narayanan et al. 2015; Cowley et al. 2017).

In high-redshift dusty galaxies, more traditional optical and ultraviolet line diagnostics are not possible due to high dust attenuation. Fine-structure transition lines such as [C II] 158 μm ($^2P_{3/2} \rightarrow {}^2P_{1/2}$) and [N II] 205 μm ($^3P_1 \rightarrow {}^3P_0$) (hereafter [C II] and [N II]) offer important insight into the properties of the interstellar medium (ISM) and importantly are not significantly affected by dust attenuation. The [C II]-to-[N II] ratio can probe physical parameters of the ISM. Assuming a pressure-equilibrium gas cloud with a range of gas densities and ionization parameters at its illuminated surface, Nagao et al. (2012) used CLOUDY modelling (Ferland et al. 1998) to show that the [C II]-to-[N II] flux ratio decreases monotonically with gas metallicity. However, because of dependences of this ratio on the unknown density and ionization parameters, additional lines such as [N II] 122 μm and [O I] 145 μm are needed to break the degeneracy with these parameters (Nagao et al. 2012). Since [C II] emission originates from both ionized and neutral gas, while [N II] is primarily emitted from ionized gas, the [C II]-to-[N II] ratio can probe the abundance of ionized and neutral gas regions in a galaxy's ISM (Decarli et al. 2014).

Several previous studies have used the [C II]-to-[N II] line ratio to investigate the ISM properties of luminous, high-redshift galaxies including SMGs (e.g. Nagao et al. 2012; Decarli et al. 2014; Béthermin et al. 2016; Pavesi et al. 2016, 2019; Umehata et al. 2017; Tadaki et al. 2019). They measure a large range in the line ratio, indicating these galaxies have diverse ISM conditions. At low redshift, Herrera-Camus et al. (2016) used [N II] 122 μm and 205 μm emission lines to constrain gas density and star formation rate (SFR), while Cormier et al. (2015) found (using the [N II] 122 μm line) that the ionized medium contributes little to the [C II] emission in their dwarf galaxy sample.

This paper presents measurements of [N II] in 40 gravitationally lensed SMGs between $3 < z < 6$ from the SPT survey. This is the first uniformly selected large sample of SMGs with [N II] detections at high redshift. When combined with 29 additional [C II] observations, these measurements allow us to make the first characterization of the high-redshift $L_{[C\,II]}/L_{[N\,II]}$ distribution in SMGs using a uniformly selected sample. Its wide redshift range makes it a unique sample to study the possible evolution in the ISM of high-redshift SMGs in comparison to local luminous infrared galaxies (LIRGs). Since the SPT galaxies are gravitationally lensed, even the relatively faint [N II] emitting sources can be detected quickly with the Morita Atacama Compact Array (ACA) of the Atacama Large Millimeter/submillimeter Array (ALMA). This allows for a complete characterization of the $L_{[C\,II]}/L_{[N\,II]}$ ratio in the ultraluminous galaxy population ($L_{FIR} > 10^{12}\,L_\odot$) at high redshift. We assume a Hubble constant $H_0 = 70\,km\,s^{-1}\,Mpc^{-1}$ and density parameters $\Omega_\Lambda = 0.7$ and $\Omega_m = 0.3$ throughout.

2 SAMPLE SELECTION, OBSERVATIONS, AND DATA REDUCTION

This sample of 40 gravitationally lensed SMGs is selected from the SPT Sunyaev–Zeldovich (SPT–SZ) survey (Vieira et al. 2010; Mocanu et al. 2013) covering 2500 deg^2 at 3, 2, and 1.4 mm wavelengths. We selected a subset of sources with $3 < z < 6$ in order to enable observation of the [N II] 205 μm line within bands 6 and 7 of ACA, including many sources that had existing [C II] observations (e.g. Gullberg et al. 2015). Each source has a secure spectroscopic redshift (Table 1) determined primarily using CO transitions and other fine-structure lines (see Strandet et al. 2016 for details).

The [N II] line observations for all sources were observed with ACA in Cycle 4 (PI: Chapman, 2016.1.00133.T), except for SPT2132–58 that was observed with the ALMA 12 m array (Béthermin et al. 2016). ACA is ideal for our measurements of the total [N II] line flux from lensed sources with large (up to ∼1.5 arcsec) Einstein radii because its FWHM beam size is 3–4 arcsec at these frequencies, with the short observations typically yielding elongated beams due to restricted UV coverage. The ACA sensitivity is still sufficient to detect this relatively faint [N II] line (compared to the much brighter [C II]) in the gravitationally lensed SMGs. The [C II] observations used here were taken with the single-dish Atacama Pathfinder Experiment (APEX) and are described in detail in Gullberg et al. (2015).

The [N II] data were reduced using the Common Astronomy Software Applications package (CASA) version 4.7 (McMullin et al. 2007). CASA's CLEAN function was used to generate continuum images and line cubes. The CLEAN depth varied depending on the source, but was between 2σ and 5σ. The typical pixel size was 1 arcsec with beam semimajor (semiminor) axes of approximately 5–7 arcsec (3–4) arcsec. Our observations of [N II] and [C II] lines are shown in Fig. 2. Our observations achieved rms continuum noise of 0.5–0.9 mJy per beam.

Fig. 1 illustrates continuum images of two of the most extended lensed SMGs in our sample, one from each of bands 6 and 7, with high-resolution ALMA band 7 continuum contours superposed. This figure illustrates that our ACA observations are unresolved even for the largest sources. To test this assumption, we extracted both continuum and line flux from elliptical aperture regions corresponding to 1× and 1.5× the beam size, in addition to a point source, single pixel extraction. These aperture extractions did not alter (or increase) the line flux measurement, indicating complete flux contained within the extraction pixel. [N II] spectral lines and the corresponding continuum were extracted at the peak of emission for all sources, with a single pixel extraction, and are shown in Fig. 2 with integrated line fluxes and luminosities given in Table 1. The continuum emission is subtracted using a zeroth-order polynomial matched to the flux baseline of off-line regions.

In Fig. 2, we plot [N II], [C II], and either CO(5–4) or CO(43) from Strandet et al. (2016), depending on redshift. In order to most

Table 1. Observed properties for our 41 SMGs ordered by μ $S_{[N\,II]}$, the observed line flux without gravitational lensing correction. The [N II] properties are determined from a single pixel extracted [N II] spectra. The instrinic flux is determined by dividing the observed flux by the gravitational lensing factor μ. Redshifts are provided from Strandet et al. (2016), while lensing models and μ values can be found in Spilker et al. (2016). For sources without lensing models, we assume our median magnification of $\mu = 6.3$ for strongly lensed SMGs (Spilker et al. 2016). Sources with model magnifications close to or equal to 1 are likely unlensed systems, some suspected to be the cores of dense protoclusters (e.g. Miller et al. 2018). Sources without a full width at half-maximum (FWHM) listed in the [C II] column do not have [C II] observations. Sources without an FWHM listed in the [N II] column have line profiles too noisy to reliably fit with a Gaussian function.

Source	z	$\mu\, S_{[N\,II]}$ [a] (Jy km s^{-1})	$SNR_{[N\,II]}$ [b]	$\mu\, L_{[N\,II]}$ ($\times 10^8\, L_\odot$)	$\mu\, S_{[C\,II]}$ (Jy km s^{-1})	$FWHM_{[N\,II]}$ (km s^{-1})	$FWHM_{[C\,II]}$ (km s^{-1})	μ
0529–54	3.3689	13.6 ± 1.7	9.3	40.4 ± 5.0	64.6 ± 7.7	415 ± 44	733 ± 81	13.2 ± 0.8
0103–45	3.0917	12.1 ± 2.3	11.7	31.2 ± 5.9	190.4 ± 23.8	429 ± 67	239 ± 39	5.1 ± 0.1
0155–62	4.349	11.6 ± 1.0	5.7	51.6 ± 4.5	26.3 ± 6.2	732 ± 104	760 ± 127	6.3 ± 1.0[c]
2146–55	4.5672	9.3 ± 0.7	12.7	44.6 ± 3.4	11.3 ± 5.8	442 ± 55	277 ± 73	6.6 ± 0.4
0113–46	4.2328	9.1 ± 0.5	8.7	38.8 ± 2.1	49.7 ± 12.8	616 ± 65	578 ± 136	23.9 ± 0.5
0532–50	3.3988	9.0 ± 0.8	7.3	27.1 ± 2.4	91.7 ± 11.2	755 ± 123	719 ± 125	10.0 ± 0.6
2357–51	3.0703	8.7 ± 1.1	7.3	22.2 ± 2.8	9.1 ± 4.6	692 ± 129	743 ± 202	2.9 ± 0.1
2037–65	4.000	8.4 ± 0.7	8.1	32.8 ± 2.7	–	503 ± 76	–	6.3 ± 1.0[c]
0109–47	3.6137	8.1 ± 1.8	9.1	26.9 ± 6.0	–	545 ± 75	–	10.2 ± 1.0
2147–50	3.7602	7.9 ± 0.6	9.1	28.0 ± 2.1	24.4 ± 7.5	570 ± 63	534 ± 104	6.6 ± 0.4
0020–51	4.1228	7.5 ± 0.6	9.4	30.7 ± 2.5	–	459 ± 66	–	4.2 ± 0.1
0027–50	3.4436	7.3 ± 0.9	8.2	22.5 ± 2.8	–	288 ± 38	–	5.1 ± 0.2
0418–47	4.2248	7.2 ± 0.6	12.5	30.6 ± 2.6	138.1 ± 10.4	366 ± 35	322 ± 37	32.7 ± 0.7
2103–60	4.4357	5.8 ± 0.6	8.7	26.6 ± 2.8	15.6 ± 10.4	670 ± 110	602 ± 204	27.8 ± 1.8
0459–59	4.7993	5.5 ± 0.8	8.2	28.5 ± 4.1	–	464 ± 63	–	4.2 ± 0.4
0551–50	3.164	5.2 ± 1.3	5.9	13.9 ± 3.5	216.1 ± 16.3	775 ± 273	734 ± 95	4.5 ± 0.5[d]
2101–60	3.156	5.0 ± 1.8	6.0	13.3 ± 4.8	9.3 ± 13.8	682 ± 273	353 ± 189	6.3 ± 1.0[c]
0136–63	4.299	4.8 ± 0.7	3.8	21.0 ± 3.1	33.3 ± 2.9	500 ± 128	526 ± 115	6.3 ± 1.0[c]
0125–50[e]	3.959	4.7 ± 0.9	4.2	18.1 ± 3.5	–	–	–	14.1 ± 0.5
0345–47	4.2958	4.4 ± 0.7	4.9	19.2 ± 3.1	15.4 ± 4.3	350 ± 75	669 ± 177	8.0 ± 0.5
2048–55	4.089	4.4 ± 1.1	3.0	17.8 ± 4.4	–	472 ± 156	–	6.3 ± 0.7
0550–53[e]	3.128	4.2 ± 1.4	4.5	11.0 ± 3.7	88.1 ± 8.6	–	789 ± 165	6.3 ± 1.0[c]
0459–58	4.856	4.1 ± 0.7	4.0	21.6 ± 3.7	–	525 ± 143	–	5.0 ± 0.6
2311–54	4.2795	3.6 ± 0.6	3.9	15.6 ± 2.6	45.3 ± 4.6	315 ± 129	352 ± 52	6.3 ± 1.0[c]
0243–49[e]	5.699	3.3 ± 0.9	3.9	22.1 ± 6.0	17.4 ± 2.7	–	796 ± 202	6.7 ± 0.5
0348–62	5.656	3.0 ± 0.6	4.8	19.9 ± 4.0	19.6 ± 3.4	507 ± 213	506 ± 132	1.2 ± 0.01
2340–59	3.864	2.6 ± 0.5	4.5	9.6 ± 1.8	48.1 ± 8.5	579 ± 198	473 ± 220	3.4 ± 0.3
0516–59	3.4045	2.6 ± 0.8	3.8	7.9 ± 2.4	–	156 ± 254	–	6.3 ± 1.0[c]
0245–63	5.626	2.4 ± 0.2	2.9	15.8 ± 1.3	26.9 ± 4.5	241 ± 83	383 ± 65	1.0 ± 0.01
2353–50	5.576	2.2 ± 0.3	2.6	14.3 ± 1.9	20.7 ± 6.4	613 ± 405	429 ± 247	6.3 ± 1.0
0300–46[e]	3.5954	2.1 ± 1.2	4.2	6.9 ± 4.0	15.7 ± 5.1	–	414 ± 237	5.7 ± 0.4
2319–55	5.2929	2.0 ± 0.8	3.9	12.0 ± 4.8	39.2 ± 4.7	339 ± 245	176 ± 28	6.9 ± 0.6
0319–47	4.51	2.0 ± 0.5	3.5	9.4 ± 2.4	11.4 ± 10.5	259 ± 42	562 ± 182	2.9 ± 0.3
2307–50	3.105	1.9 ± 0.6	3.2	4.9 ± 1.6	–	~98	–	6.3 ± 1.0[c]
2132–58[f]	4.7677	1.7 ± 0.2	11.5	8.9 ± 0.8	35.9 ± 6.9	245 ± 16	212 ± 43	5.7 ± 0.5
0441–46	4.4771	1.5 ± 0.5	2.9	7.0 ± 2.3	26.3 ± 5.8	393 ± 106	546 ± 123	12.7 ± 1.0
2349–56	4.304	1.1 ± 0.5	2.9	4.8 ± 2.2	–	–	–	1.0
0202–61	5.018	0.036[g]	4.5	–	19.3 ± 4.1	~60	771 ± 325	9.1 ± 0.07
0346–52	5.6559	>0.9	2.9	>6.0	64.1 ± 8.2	~64	486 ± 85	5.6 ± 0.1
2052–56	4.257	0.1 ± 0.4	2.3	0.4 ± 1.7	14.6 ± 1.8	~91	382 ± 122	1.0
2351–57	5.811	>−0.8	2.7	>−5.5	5.4 ± 2.7	383 ± 409	539 ± 82	6.3 ± 1.0[c]

[a]Errors quoted are rms from the 1D spectra.
[b]Signal-to-noise ratio determined from the source peak in *uv*-plane continuum-subtracted channel maps.
[c]$\mu = 6.3$ is assumed. No lensing model.
[d]Lens model by K. Sharon (private communication).
[e]The [N II] spectra for these sources do not have sufficient baseline to completely cover the CO line profile. The fluxes quoted for [N II] and [C II] are truncated to the [N II] spectral coverage.
[f]From Béthermin et al. (2016).
[g]Positive flux measurement from channel map (Jy per beam). Our procedure for measuring total flux results in a negative value for this source.

reliably determine the integrated fluxes in both [N II] and [C II], we use the $FWHM_{CO}$ of the high SNR CO lines to determine the velocity range over which to sum our [N II] and [C II] detections. We first fit the CO line profiles with a single Gaussian function and then use this to obtain our line flux measurements by summing [N II] and [C II] over a velocity range $2 \times FWHM_{CO}$, covering the full width of our [N II] line profiles. For brighter [N II] sources, we confirmed through a curve of growth analysis that this represents >95 per cent of the line flux, while for fainter [N II] sources this avoids large variations in the line flux measurement from integrating noise fluctuations outside the line frequencies. For sources with both [N II] and [C II] observations, we compared the FWHM determined

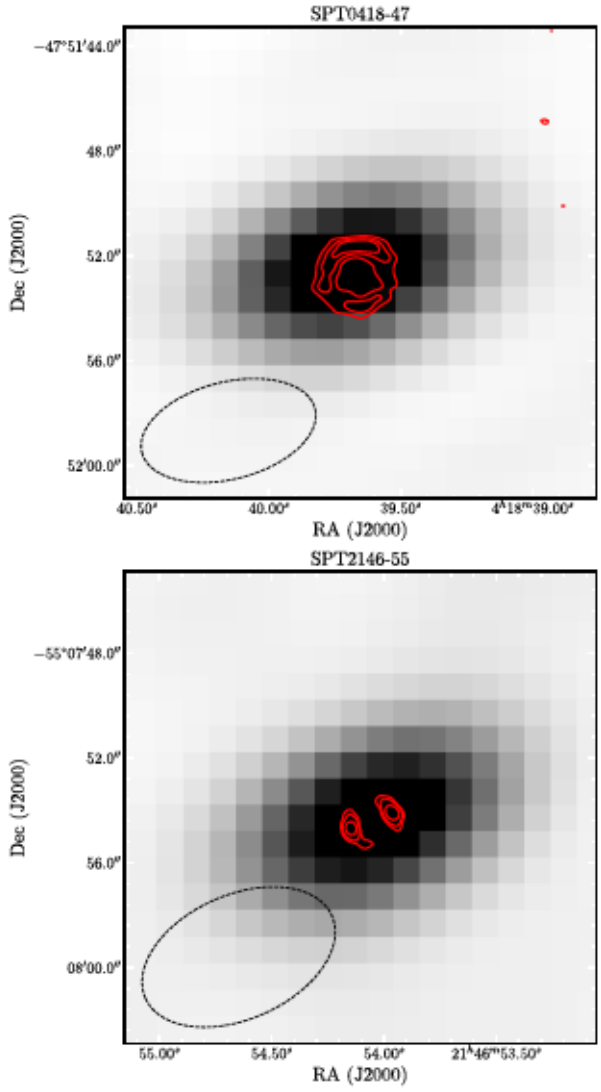

Figure 1. Two examples of our ALMA ACA [N II] line observations, one from each of bands 6 and 7, showing the [N II] detection as a channel map optimized over the FWHM of the line in grey-scale. The red contours represent continuum from higher resolution band 7 ALMA imaging, and demonstrate that the ACA beam does not resolve even the largest lensed SMGs in our sample. The beam size is represented in the bottom left corner by the black dashed line ellipse. Top panel: [N II] observations of SPT0418–47 in band 7. Bottom panel: [N II] observations of SPT2146–55 in band 6.

from a Gaussian fit for each line. Over the full sample, there is a good one-to-one agreement between these two line widths, although the relatively low SNRs of many of the lines (both [N II] and [C II]) result in significant scatter in the relation.

We fit the [N II] line profiles and compare to the [C II] profiles, both listed in Table 1. In 4 of the 40 cases, our spectral bandwidth only covers between 50 and 70 per cent of the CO-defined line (SPT0125–50, SPT0300–46, SPT0243–49, and SPT0550–53). This was a compromise taken in order to attempt to reduce the overall project calibration overhead, since the total project exceeded 50 h. In these cases, we only sum the [C II] line to the end of the [N II] line coverage. The [N II] and [C II] fluxes, along with the observed [N II] luminosities, are presented in Table 1. In Fig. 3, the demagnified [N II] luminosities, are plotted against demagnified $L_{\rm FIR}$ and $T_{\rm dust}$, using magnification values (μ) from Spilker et al. (2016).

3 RESULTS

We robustly detect [N II] lines with the ACA at $>4.5\sigma$ in 22 of our sample of 41 SMG observations (including SPT2132–58 from Béthermin et al. 2016), with a further 13 sources detected at $\geq 3\sigma$. The $>4.5\sigma$ criterion results in a 5 per cent false-positive chance in our data, which drops to less than 1 per cent chance when the measurement is constrained to within one-half beam of the CO-source coordinates. These lines are detected at the redshifted velocity expected based on redshifts presented in Strandet et al. (2016). Along with the 11.5σ [N II] detection of SPT2132–58 (Béthermin et al. 2016), this represents a total of 35 detections in the sample of 41. In the six sources with undetected [N II], an upper limit was estimated as 3× the channel rms in the central pixel at velocities away from the line. For our lines with $\sigma \geq 3$, we find magnified [N II] line fluxes ranging between approximately 1 and 14 Jy km s^{-1} and [C II] flux between 5 and 216 Jy km s^{-1}. These correspond to [N II] line luminosities of ($\sim$5–40) × 10^8 L$_\odot$, and detected $L_{\rm [C\,II]}/L_{\rm [N\,II]}$ line luminosity ratios over two orders of magnitude. The sample has an interquartile range in line luminosity ratios $L_{\rm [C\,II]}/L_{\rm [N\,II]}$ of 5.0–24.7 and a median of 11.0 (see Fig. 3, rightmost panel for a histogram detailing this distribution). These statistical values are calculated by treating the $L_{\rm [C\,II]}/L_{\rm [N\,II]}$ lower limits ([N II] non-detections) as real measured values at the measured limit.

To properly account for the lower limits in $L_{\rm [C\,II]}/L_{\rm [N\,II]}$, we perform survival analysis using the LIFELINES PYTHON package (Davidson-Pilon et al. 2018). Survival analysis is often used to determine the time until an event occurs. In cases where an event is not precisely observed, the last observation made before the event occurs can still be used as a lower limit in calculating statistical quantities. For our line ratios, we utilize the lower limits as the last observation before the 'event' occurs, where the event is the true line ratio. This analysis gives a slightly lower median value of 9.7 with a similar interquartile range of 5–25. Furthermore, reducing our sample to include only sources with good quality [N II] and [C II] detections did not significantly alter our measured medians or interquartile ranges.

In the majority of our sources (17/30, or $\sim$60 per cent), the $L_{\rm [C\,II]}/L_{\rm [N\,II]}$ luminosity ratio (or lower limit) corresponds to model expectations from X-ray dominated regions (XDR), photon dominated regions (PDR) or shock regions determined by Decarli et al. (2014). Decarli et al. (2014) use $L_{\rm [C\,II]}/L_{\rm [N\,II]} \sim 2$ for H II regions and greater than $L_{\rm [C\,II]}/L_{\rm [N\,II]} \sim 9$ for PDR/XDR regions (see Fig. 3). Three SPT SMGs fall well within the range expected for H II-dominated regions (with another three overlapping within error or as a lower limit), with the rest existing in an intermediate region, or more balanced regime in between the ionized gas-dominated and PDR/shock-dominated regions. Galaxies with [C II]/[N II] ratios in the XDR/PDR or shock region regime are expected to have [N II] emission originating predominantly from H II regions with [C II] emission originating from both H II regions and the outer layers of PDRs (Béthermin et al. 2016).

We assembled a sample of $L_{\rm [C\,II]}/L_{\rm [N\,II]}$ in local LIRGs from Díaz-Santos et al. (2017), Lu et al. (2017), and Zhao et al. (2016). To investigate whether the SPT SMG sample and the local LIRGs arise from different underlying distributions of $L_{\rm [C\,II]}/L_{\rm [N\,II]}$, we perform a two-sample Kolmogorov–Smirnov (KS) test and t-test. The KS test yields a P-value of 0.44, while the t-test yields $P = 0.36$. These test results prevent us from conclusively determining the line ratios coming from different underlying distributions. In our literature sample, when dust temperatures were not available they

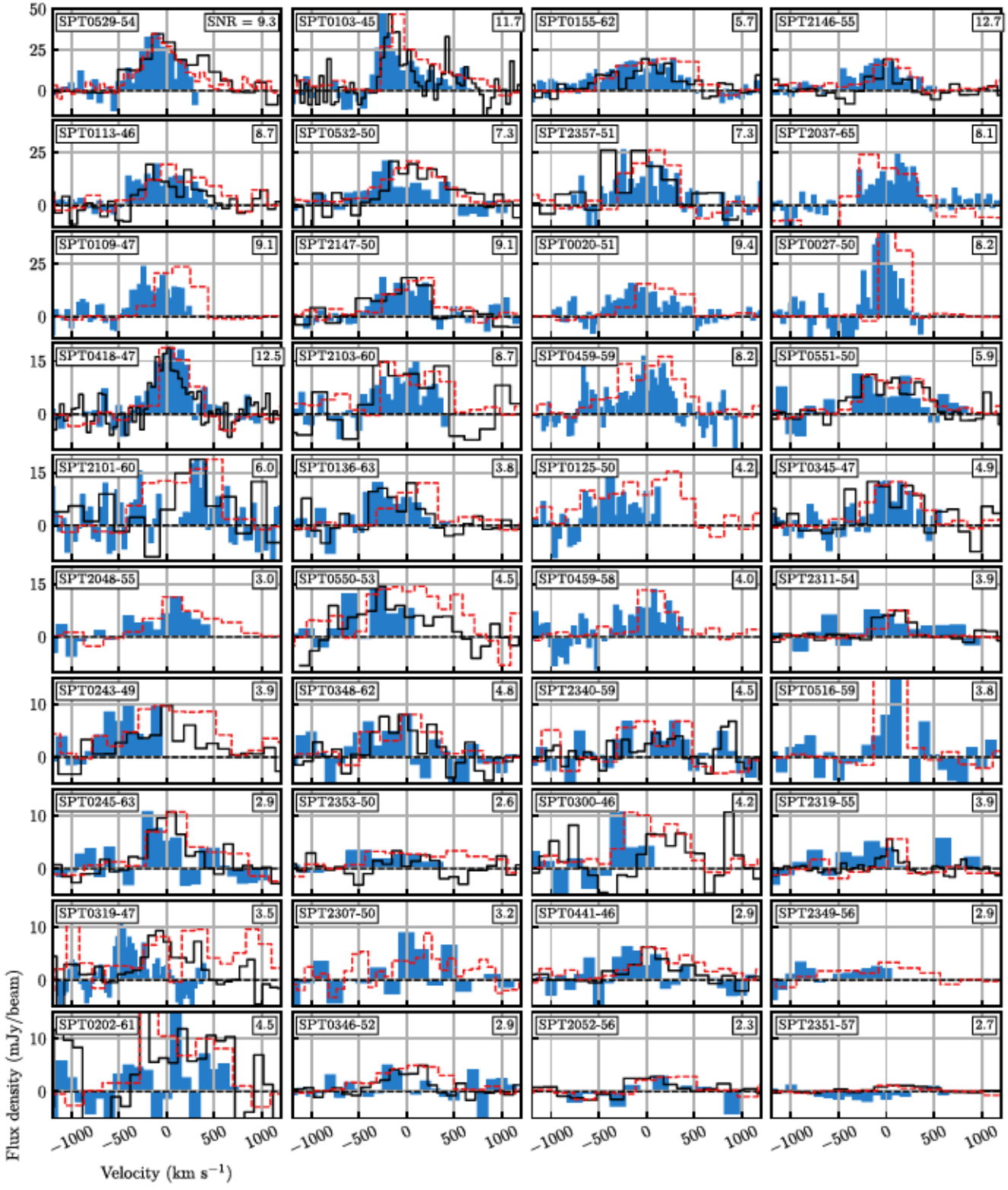

Figure 2. Observed [N II] 205 μm (blue background), [C II] 158 μm (black line), and CO (dashed red line) line profiles for the 40 ALMA observed sources, excluding SPT2132–58 that was presented in Béthermin et al. (2016). Sources are ordered by observed [N II] 205 μm flux, given in Table 1. The [N II] spectra are single pixel extractions. The SNR from the optimal integrated line detection is given in the upper right corner of each panel. The CO line is either CO(4–3) or CO(5–4) depending on source redshift (see Strandet et al. 2016). Both CO and [C II] lines are normalized to the peak [N II] flux for each source (see Table 1 for [C II] flux). The zero velocity is determined according to redshifts presented in Strandet et al. (2016).

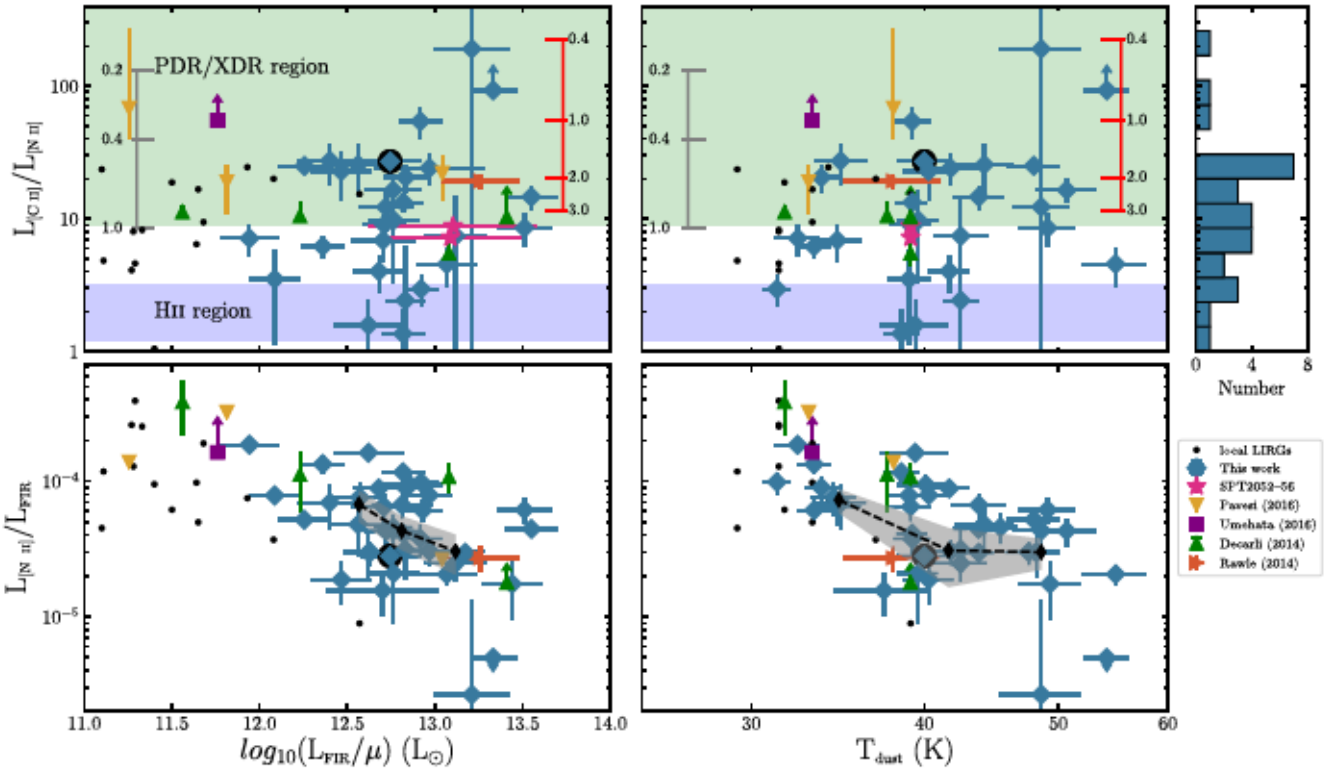

Figure 3. Comparison of key properties of our lensed sample of [N II] and [C II] observations (shown in blue diamonds) with literature measurements. Top panels: Observed $L_{[C\,II]}/L_{[N\,II]}$ plotted against demagnified L_{FIR} and dust temperature. Expected $L_{[C\,II]}/L_{[N\,II]}$ regimes for H II and photon or x-ray dominated regions based on Decarli et al. (2014) are shown. Modelled metallicity grids for ISM densities of $\log(n) = 1.5$ (grey) and 3.0 (red), each with ionization parameter $\log(U_{H\,II}) = -3.5$, are shown as floating axes (Nagao et al. 2012) with metallicity units of $Z/Z_\odot$. Bottom panels: Observed L_{FIR} normalized [N II] luminosities. The black diamonds and the grey shaded regions in the bottom panels represent the binned medians and errors of demagnified L_{FIR} normalized [N II] luminosities and dust temperature. For literature sources, the upwards green triangles represent sources from Decarli et al. (2014): two Lyman alpha emitters, an SMG, and a quasar in order of increasing L_{FIR} at $z = 4.7$. The downwards yellow triangles represent Pavesi et al. (2016) sources, which are LBG-1 (typical Lyman-break galaxy), HZ10 (FIR-luminous LBG), and AzTEC-3 (a massive SMG) in order of increasing L_{FIR} at $z = 5.3$–5.65. The purple square represents LAB1-ALMA3, a galaxy embedded in a Lyman alpha blob at $z = 3.1$ (Umehata et al. 2017). A SMG (rightward orange triangle) at $z = 5.243$ from Rawle et al. (2014) and two components of SPT2052–56, an unlensed protocluster of SMGs at $z = 4.3$, are also shown (pink stars – Pass et al., in preparation). SPT2132–58 (Béthermin et al. 2016) has a black circular background. Local LIRGs assembled from Lu et al. (2017), Díaz-Santos et al. (2017), and Zhao et al. (2016) are shown as small black dots.

were estimated using the relationship shown in Symeonidis et al. (2013).

We investigate the relationship between $L_{[N\,II]}/L_{FIR}$ versus L_{FIR} (42.5–122.5 μm) by binning our sources according to L_{FIR}. We divide our sources with $L_{[N\,II]}$ measurements into three bins of roughly equal size, ranging from $\log_{10}(L_{FIR}) = [<12.71, 12.71$–$12.9, >12.9]$. From smallest to largest bins, we measure $L_{[N\,II]}/L_{FIR}$ of $\sim 6.8 \times 10^{-5}$, 4.3×10^{-5}, and 3.0×10^{-5}. These bins and their medians (and errors) are shown as black diamonds and grey shaded regions in the lower left-hand panel of Fig. 3.

We also investigate the trend between dust temperature and $L_{[N\,II]}/L_{FIR}$. These results are presented in the bottom right-hand panel of Fig. 3, where we plot $L_{[N\,II]}/L_{FIR}$ against T_{dust}. We also bin our sources into three bins of roughly equal number according to dust temperature: $T_{dust} = [<39.3, 39.3$–$43.8, >43.8]$. These bins have median values $L_{[N\,II]}/L_{FIR}$ of $\sim 7.3 \times 10^{-5}$, 3.1×10^{-5}, and 3.0×10^{-5}.

4 DISCUSSION

Our [N II] observations for a sample of 40 SMGs at $z = 3 - 6$ represent the largest uniformly selected sample of high-redshift [N II] detections to date. In our 30 sources with both [N II] and [C II] observations, we are able to characterize the $L_{[C\,II]}/L_{[N\,II]}$ out to the high redshifts probed by our SMG sample, and in over a decade range in (demagnified) far-IR luminosity ($\sim 12 < \log_{10}(L_{FIR}/\mu) < 13.5$). This has allowed us to capture the true $L_{[C\,II]}/L_{[N\,II]}$ range for luminous, dusty galaxies, and better understand the outliers to the distribution.

All previous literature measurements of $L_{[C\,II]}/L_{[N\,II]}$ in distant, far-IR luminous galaxies are found to lie within the range of $L_{[C\,II]}/L_{[N\,II]}$ ratios we observe in the SPT SMGs. The SPT SMGs exhibit among the highest and lowest ratios yet seen in high redshift, FIR luminous galaxies. However, our measurements also detect a population of high-redshift SMGs that have lower $L_{[C\,II]}/L_{[N\,II]}$ ratios than shown in the previous literature. We find 8 of our 30 SMGs have $L_{[C\,II]}/L_{[N\,II]}$ values (or are consistent within error) suggesting a hybrid regime between the model predictions of PDR/XDR emission and H II regions. These sources suggest neither H II regions nor PDR/XDR regions dominate the [C II] flux. Instead, the [C II] flux has significant contributions from both regions. The $L_{[C\,II]}/L_{[N\,II]}$ in these sources cannot be explained as originating in only H II regions – both neutral and ionized gas must contribute to the total [C II] 158 μm luminosity. SMGs lying in this hybrid

or even H II-dominated regimes could represent very enriched, high-metallicity gas in combination with low gas densities, and appropriate ionization parameters. The C/N abundance ratio may vary as a function of metallicity (e.g. Nagao et al. 2012), and could be an important contributor to the $L_{[C\,II]}/L_{[N\,II]}$ line ratio. These SMGs may also have very high masses of ionized gas relative to the molecular gas fraction. Detailed multiline studies of these sources will be undertaken in follow-up contributions to better understand this unusual situation for such massive and dusty star-forming galaxies.

At the highest values of $L_{[C\,II]}/L_{[N\,II]}$, we detect five sources with larger ratios than the previous SMG record holder SPT2132–58 (Béthermin et al. 2016), and comparable to the lower far-IR luminous sources of Umehata et al. (2017) and Pavesi et al. (2016). These sources likely represent extreme ISM environments, where total [C II] emission is dominated by the contribution from PDR/XDR regions. Since neutral nitrogen has a higher ionization potential than hydrogen, we expect that [N II] 205 μm emission will only originate in ionized gas. Therefore, our sources with extremely high $L_{[C\,II]}/L_{[N\,II]}$ may have a relatively low contribution to [C II] from ionized gas where the [N II] originates.

Comparing our SMG sample to local LIRGs, we observe slightly higher $L_{[C\,II]}/L_{[N\,II]}$ values, possibly owing to lower density gas and therefore a lower contribution of [C II] emission from PDR/XDR regions in local (U)LIRGs. However, the p-values from both the t-test and KS test (see Section 3) suggest we cannot say the SMGs and local LIRGs arise from different underlying distributions.

We follow the analysis of Nagao et al. (2012) and include two metallicity grids for gas densities of $\log(n) = 1.5$ and $= 3$, each with ionization parameter $\log(U) = -3.5$ in Fig. 3. According to the models of Nagao et al. (2012), higher $L_{[C\,II]}/L_{[N\,II]}$ should originate in lower metallicity environments. In our sample, we see that the majority of our sample of galaxies have line ratios that place them in the metallicity range of $0.6 < Z/Z_{\odot} < 3.0$ if we assume $\log(n) = 3$. Assuming $\log(n) = 1.5$, we find metallicities in the range $0.2 < Z/Z_{\odot} < 1.0$. In both cases, the metallicity spans sub- to solar or supersolar ranges. However, direct interpretation of $L_{[C\,II]}/L_{[N\,II]}$ in terms of metallicity is undermined by unconstrained gas density, elemental abundances, fractional abundance of ionized and neural gas, and ionization parameter, which can also affect this luminosity ratio (e.g. Nagao et al. 2012; Pavesi et al. 2016). In galaxies with a significant fraction of neutral ISM, [C II] emission will more heavily outweigh [N II] than in galaxies with a significant ionized ISM component.

We investigate the relationship between $L_{[N\,II]}/L_{FIR}$ versus T_{dust}. We observe a deficit in $L_{[N\,II]}/L_{FIR}$ towards higher T_{dust} after binning according to dust temperature. Gullberg et al. (2015) similarly observed decreasing $L_{[C\,II]}/L_{FIR}$ towards increasing dust temperature. This result was first presented and explained in Malhotra et al. (2001) who explained this ratio may change due to one of two reasons: (1) high far-ultraviolet flux to gas density ratios may positively charge dust grains and therefore decrease heating efficiency, or (2) softer radiation fields can be less effective in heating gas and instead heat only the dust. Gullberg et al. (2015) acknowledged the Stefan–Boltzmann law may explain part of this dependence, as $L_{FIR} \propto T_{dust}^4$. To cancel this relationship, we plot $(L_{[N\,II]}/L_{FIR})\times(T_{dust}/40\ K)^4$ versus T_{dust} in Fig. 4. After removing this dependence, we perform a Kendall tau test on the sample and calculate a P-value of 0.49. Similarly to the results presented in Gullberg et al. (2015), this result means we neither confirm the existence of a correlation between these variables nor confirm that [N II] emission is largely independent of dust temperature for our SPT SMGs. To investigate whether the trend appears in sources depending on the relative significance of [N II] emission, we reduce the sample into two sub-samples according to their $L_{[C\,II]}/L_{[N\,II]}$. We define the [N II] significant sources as those with $L_{[C\,II]}/L_{[N\,II]} < 10$, and the [N II] insignificant sources with $L_{[C\,II]}/L_{[N\,II]} > 10$. For these samples, we repeat the Kendall tau test and calculate P-values of 0.17 and 0.08, respectively. This indicates our sources with significant ionized gas emission $L_{[C\,II]}/L_{[N\,II]} < 10$ do not exhibit a correlation between $L_{[N\,II]}/L_{FIR}$ and T_{dust}, nor do sources with more significant PDR/XDR region emission.

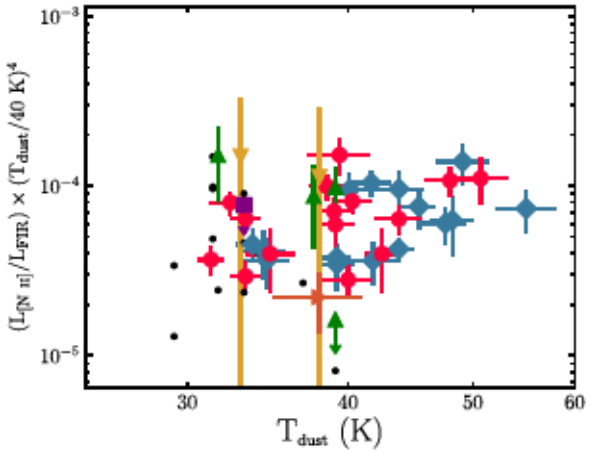

Figure 4. The distribution of $(L_{[N\,II]}/L_{FIR})\times(T_{dust}/40\,K)^4$ versus T_{dust}. We plot SPT SMGs in blue diamonds and red circles. Blue diamonds represent sources with $L_{[C\,II]}/L_{[N\,II]} > 10$, and red circles represent $L_{[C\,II]}/L_{[N\,II]} < 10$. This allows us to investigate whether sources with more significant [N II] emission exhibit a relationship between $L_{[N\,II]}/L_{FIR}$ and dust temperature. The other souces utilize the same legend as Fig. 3.

5 CONCLUSIONS

We have presented the first uniformly selected sample of high-redshift [N II] 205 μm observations and utilized previous observations of the [C II] 158 μm line to probe the ISM. We summarize our main conclusions here:

(i) We find that our SPT SMGs have a wide distribution of $L_{[C\,II]}/L_{[N\,II]}$. The median $L_{[C\,II]}/L_{[N\,II]}$ is 11.0 with an interquartile range of 5.0–24.7. Using survival statistics to account for our lower limits did not significantly alter our results. This resulted in a median of 9.7 and an interquartile range of 5–25.

(ii) We measure a decrease in $L_{[N\,II]}/L_{FIR}$ towards increasing L_{FIR}. From the lowest luminosity bin ($\log_{10}(L_{FIR}) < 12.71$) to our highest luminosity bin ($\log_{10}(L_{FIR}) > 12.9$), we find medians of $\sim 6.8\times10^{(-5)}$ decreasing to $\sim 3.0\times10^{(-5)}$.

(iii) We cannot determine whether our measured [N II] emission is independent of dust temperature, after cancelling the $L_{FIR} \propto T_{dust}^4$ dependence and performing a Kendall tau correlation test, including samples with high and low $L_{[C\,II]}/L_{[N\,II]}$ values.

(iv) Our range in observed $L_{[C\,II]}/L_{[N\,II]}$ can be explained through variations in gas density, ionization parameter, and metallicity. We note that further observations of fine-structure lines such as [N II] 122 μm and [O I] 145 μm will help break the degeneracy of the $L_{[C\,II]}/L_{[N\,II]}$ on gas density and ionization parameter (Nagao et al. 2012), and will help strengthen conclusions based on comparisons of the [C II]-to-[N II] ratio between local LIRGs and the high-redshift Universe.

ACKNOWLEDGEMENTS

This paper used the following ALMA data: ADS/JAO.ALMA#2016.1.00133.T. ALMA is a partnership of ESO (representing its member states), NSF (USA), and NINS (Japan), together with NRC (Canada), MOST and ASIAA (Taiwan), and KASI (Republic of Korea), in cooperation with the Republic of Chile. The Joint ALMA Observatory is operated by ESO, AUI/NRAO, and NAOJ.

The SPT is supported by the National Science Foundation (NSF) through grant PLR-1248097, with partial support through PHY-1125897, the Kavli Foundation, and the Gordon and Betty Moore Foundation grant GBMF 947. DPM, JDV, KCL, and SJ acknowledge support from the US NSF under grants AST-1715213 and AST-1716127. SJ and KCL acknowledge support from the United States (US) National Science Foundation (NSF) National Radio Astronomy Observatory (NRAO) under grants SOSPA5-001 and SOSPA4-007, respectively. JDV acknowledges support from an A. P. Sloan Foundation Fellowship.

The National Radio Astronomy Observatory is a facility of the National Science Foundation operated under cooperative agreement by Associated Universities, Inc.

DJMC and SCC acknowledge the support of the Natural Sciences and Engineering Research Council of Canada (NSERC).

REFERENCES

Béthermin M. et al., 2016, A&A, 586, L7
Casey C. M., Narayanan D., Cooray A., 2014, Phys. Rep., 541, 45
Chapman S. C., Blain A. W., Ivison R. J., Smail I. R., 2003, Nature, 422, 695 EP
Chapman S. C., Blain A. W., Smail I., Ivison R. J., 2005, ApJ, 622, 772
Cormier D. et al., 2015, A&A, 578, A53
Cowley W. I., Béthermin M., Lagos C. d. P., Lacey C. G., Baugh C. M., Cole S., 2017, MNRAS, 467, 1231
Davidson-Pilon C. et al., 2018, CamDavidsonPilon/lifelines: v0.14.6
Decarli R. et al., 2014, ApJ, 782, L17
Díaz-Santos T. et al., 2017, ApJ, 846, 32
Ferland G. J., Korista K. T., Verner D. A., Ferguson J. W., Kingdon J. B., Verner E. M., 1998, PASP, 110, 761
Gullberg B. et al., 2015, MNRAS, 449, 2883
Hainline L. J., Blain A. W., Smail I., Alexander D. M., Armus L., Chapman S. C., Ivison R. J., 2011, ApJ, 740, 96
Hayward C. C., Narayanan D., Kereš D., Jonsson P., Hopkins P. F., Cox T. J., Hernquist L., 2013, MNRAS, 428, 2529
Herrera-Camus R. et al., 2016, ApJ, 826, 175
Lu N. et al., 2017, ApJSS, 230, 1
Ma J. et al., 2015, ApJ, 812, 88
Malhotra S. et al., 2001, ApJ, 561, 766
McMullin J. P., Waters B., Schiebel D., Young W., Golap K., 2007, in Shaw R. A., Hill F., Bell D. J., eds, ASP Conf. Proc. Vol. 376, Astronomical Data Analysis Software and Systems XVI. Astron. Soc. Pac, San Francisco, p. 127
Michalowski M. J., Dunlop J. S. Cirasuolo M., Hjorth J. Hayward C. C., Watson D., 2012, A&A, 541, A85
Miller T. B. et al., 2018, Nature, 556, 469
Mocanu L. M. et al., 2013, ApJ, 779, 61
Nagao T., Maiolino R., De Breuck C., Caselli P., Hatsukade B., Saigo K., 2012, A&A, 542, L34
Narayanan D. et al., 2015, Nature, 525, 496 EP
Pavesi R. et al., 2016, ApJ, 832, 151
Pavesi R., Riechers D. A., Faisst A. L., Stacey G. J., Capak P. L., 2019, ApJ, 882, 168
Rawle T. D. et al., 2014, ApJ, 783, 59
Shimizu I., Yoshida N., Okamoto T., 2012, MNRAS, 427, 2866
Spilker J. S. et al., 2016, ApJ, 826, 112
Strandet M. L. et al., 2016, ApJ, 822, 80
Swinbank A. M. et al., 2014, MNRAS, 438, 1267
Symeonidis M. et al., 2013, MNRAS, 431, 2317
Tadaki et al., 2019, ApJ, 876, 1
Umehata H. et al., 2017, ApJ, 834, L16
Vieira J. D. et al., 2010, ApJ, 719, 763
Wardlow J. et al., 2011, MNRAS, 415, 1479
Weiß A. et al., 2013, ApJ, 767, 88
Zhao Y. et al., 2016, ApJ, 819, 69

This paper has been typeset from a TEX/LATEX file prepared by the author.